

## ARTICLE OPEN



# Weave-pattern-dependent fabric piezoelectric pressure sensors based on polyvinylidene fluoride nanofibers electrospun with 50 nozzles

Da Bin Kim<sup>1,7</sup>, Ju Han<sup>1,7</sup>, Sun Min Sung<sup>2,7</sup>, Min Seong Kim<sup>2</sup>, Bo Kyoung Choi<sup>2</sup>, Sung Jun Park<sup>1</sup>, Hyae Rim Hong<sup>1,3</sup>, Hong Je Choi<sup>1,4</sup>, Byeong Kon Kim<sup>1,5</sup>, Chung Hee Park<sup>3</sup>, Jong Hoo Paik<sup>6</sup>, Joon-Seok Lee<sup>2</sup>✉ and Yong Soo Cho<sup>1</sup>✉

Wearable pressure sensors having versatile device structures have been extensively investigated to achieve high sensitivity under mechanical stimuli. Here, we introduce piezoelectric pressure sensors based on fabrics woven using polyvinylidene fluoride (PVDF) weft and polyethylene terephthalate (PET) warp yarns with different weave structures: 1/1 (plain), 2/2, and 3/3 weft rib patterns. The dependence of the pressure-sensing performance on the weave pattern is demonstrated with an actual large-scale fabric up to the ~2 m scale. An optimized pressure sensor with a 2/2 weft rib pattern produced a high sensitivity of  $83 \text{ mV N}^{-1}$ , which was 245% higher than that of the 1/1 pattern. The detection performance of the optimal fabric was extensively evaluated with a variety of ambient input sources, such as pressing, bending, twisting, and crumpling, as well as various human motions. Further, a large all-fabric pressure sensor with arrayed touch pixel units demonstrated highly sensitive and stable sensing performance.

*npj Flexible Electronics* (2022)6:69; <https://doi.org/10.1038/s41528-022-00203-6>

## INTRODUCTION

Piezoelectricity in asymmetric materials has been extensively explored in the last few decades to efficiently extract electrical energy through electromechanical energy conversion<sup>1–3</sup>. Although piezoelectricity-driven power generation devices create instantaneous energy only after being stimulated by a mechanical input, the merit of these devices lies in utilizing free mechanical sources, thus providing a unique energy alternative for electronic components that consume low power<sup>4–6</sup>. Depending on the specific application requirements, appropriate materials, device structure, and processing are critical to producing highly efficient sensing devices based on the electromechanical coupling<sup>7–10</sup>. In addition to the typical inorganic materials having high piezoelectricity, resilient organic materials with reliable mechanical flexibility have been examined as alternative candidates for wearable devices with excellent power outcomes<sup>11–13</sup>. In this regard, piezoelectric polymers, such as poly(vinylidene fluoride) (PVDF) or its derivatives, are the most promising materials because of their wide availability and processing adaptability along with strong piezoelectricity<sup>14–17</sup>. The polymers have been used mostly in the form of macro- or nanofibers, typically processed by electrospinning at a high electric field, which is responsible for the in situ formation of polar  $\beta$ -phase<sup>18,19</sup>. The electrospinning process is suitable for the large-scale production of nanofibers with adjustable diameters from nano- to micron-scale, while the textile with thinner fibers provides high mechanical flexibility with good air permeability<sup>15,20,21</sup>. In particular, nanofiber structures have been extensively investigated for use in highly efficient piezoelectric energy harvesters with structural modifications<sup>22–26</sup>. Specifically, for wearable applications, piezoelectric polymer nanofibers are useful for ultimately creating a fabric-type device

structure, ensuring highly adaptable electromechanical power generation with mechanical resilience in various environments<sup>27–33</sup>. For example, PVDF fibers were further processed by drawing and twisting into a yarn to fabricate a fabric for various piezoelectric applications such as generators and sensors<sup>28–31</sup>. A piezoelectric energy harvester was assembled from fabric based on PVDF yarn, and it showed a peak voltage of 0.14 V and a sensitivity of  $28 \text{ mV N}^{-1}$  under compression after poling at an electric field of  $\sim 2.7 \text{ V } \mu\text{m}^{-1}$ <sup>27</sup>. Meanwhile, a pressure-sensitive fabric was woven from poly(3,4-ethylene dioxythiophene) (PEDOT)-coated PVDF yarns in both the warp and weft directions, with the resulting sensitivity of up to  $18.4 \text{ kPa}^{-1}$  at a pressure of  $100 \text{ Pa}$ <sup>32</sup>. However, most of the fabric studies have used the melt-spinning process necessitating extra poling with less dimensional controllability, whereas conventional electrospinning has rarely been demonstrated to fabricate twisted yarns through a continuous process. In addition, only limited studies have achieved a relatively high sensitivity under applied input forces without applying any post-treatment to the fabric.

Herein, we propose a fabric generator incorporating PVDF nanofiber yarns that are produced by a sequential process, involving 50-nozzle-electrospinning at high fields, drawing, and twisting during the yarning process. Using commercial polyethylene terephthalate (PET) yarns, different weave structures such as 1/1 (plain), 2/2, and 3/3 weft rib patterns were created. For example, the PVDF yarn was woven in the weft direction, whereas the PET yarn was woven in the warp direction to form different weaving patterns. The PET warp yarn was selected to secure the mechanical integrity with the PVDF weft with the recognition of inexpensive PET as one of the most popular yarns in the fabric and textiles<sup>34</sup>. PET is known to possess remarkable mechanical

<sup>1</sup>Department of Materials Science and Engineering, Yonsei University, Seoul 03722, Republic of Korea. <sup>2</sup>Department of Textile Engineering and Technology, Yeungnam University, Gyeongsan 38541, Republic of Korea. <sup>3</sup>Department of Textile, Merchandising and Fashion Design, Seoul National University, Seoul 08826, Republic of Korea. <sup>4</sup>Samsung Electro-Mechanics Co. Ltd., Suwon 16674, Republic of Korea. <sup>5</sup>Ceratoq Inc., Seoul 08511, Republic of Korea. <sup>6</sup>Electronic Materials and Component Center, Korea Institute of Ceramic Engineering and Technology, Jinju 52851, Republic of Korea. <sup>7</sup>These authors contributed equally: Da Bin Kim, Ju Han, Sun Min Sung. ✉email: [leejs@ynu.ac.kr](mailto:leejs@ynu.ac.kr); [ycho@yonsei.ac.kr](mailto:ycho@yonsei.ac.kr)

properties, such as high tensile strength of 925 MPa and Young's modulus of 16 GPa<sup>35</sup>.

In addition, the nanofibers were aligned by an array of intermittent Cu rods on the conveyor during electrospinning. The performance of the PVDF/PET weave patterns under periodic compression was optimized in terms of their power-generation capability, and the optimal pattern of a 2/2 weft rib weave delivered an impressive sensitivity of 83 mV N<sup>-1</sup>. In addition, the fabric effectively detected electrical signals of up to a few nanoamperes under various physiological mechanical sources, such as twisting, crumpling, finger bending, walking, and running. A pressure sensor array was also successfully patterned on a large-area fabric, demonstrating its potential for wearable self-powered electronic devices in a production scale.

## RESULTS

### Large-area PVDF nanofiber-based fabrics

Figure 1a presents a schematic of electrospinning process using 50 nozzles. The key technical aspect was the use of 50 nozzles to continuously produce an aligned nanofiber mat using a rotating belt toward the other end of the conveyor. In particular, parallel Cu rods were placed on the belt conveyor at an interval of 1.5 cm to aid the alignment of the spun fibers via electrostatic interactions. The effect of Cu for fiber alignment was reported previously specifically when the parallel Cu wires were arrayed on a drum of the fiber collector<sup>36–38</sup>. The existence of Cu makes the nanofibers experience the electrostatic force between an incoming section of charged fiber and charges on the surfaces of fibers attached to the Cu, resulting in the stretched fibers across the short distance between the Cu rods and thus the alignment of fibers. Apart from the assistance of Cu rods for alignment, the

long-range alignment of the nanofibers was secured along the pulling direction as the electrospun PVDF nanofibers were pulled from the other end of the conveyor by a rotating drum. As shown in the SEM image in Fig. 1b, well-aligned fibers were assured. It is necessary to align fibers to achieve effective stretching (for piezoelectricity) and high mechanical integrity along the length of the fiber<sup>39</sup>. The diameter of the fibers ranged mostly between ~700 and ~1300 nm, with an average diameter of 973 nm, as shown in the fiber size distribution (Fig. 1b). The effects of the rotating belt and Cu rods during electrospinning on the fiber alignment are further presented in Supplementary Fig. 1, in which the degree of alignment was evaluated using contour and peak plots of the fast Fourier transform (FFT)<sup>36</sup>. For example, the aligned fibers appear well oriented in the SEM images and corresponding FFT (Supplementary Fig. 1c, e), with two major peaks at approximately 90° and 270° because the fibers align in this direction with elliptically distributed pixels. In contrast, the randomly oriented PVDF nanofibers did not exhibit major peaks, as shown in Supplementary Fig. 1f.

A single-filament yarn was fabricated by sequential cold drawing, setting, and twisting of the as-spun nanofiber mat and then the four-ply yarn was finally made by twisting four single-filament yarns. The number of twists per unit length for the four-ply yarn varied from 50 to 500 twists per meter (TPM), as shown in the SEM image of Fig. 1c for the four-ply yarn twisted at 300 TPM as an example. Figure 1a also schematically illustrates the three weave patterns fabricated using two different yarns, a four-ply PVDF yarn and a common PET yarn, by a commercial weaving machine. The three different patterns correspond to the 1/1, 2/2, and 3/3 weft rib structures, in which the PVDF and PET yarns were used as the weft (horizontal) and warp (vertical), respectively. In these patterns, the weft and warp yarns alternately crossed up and

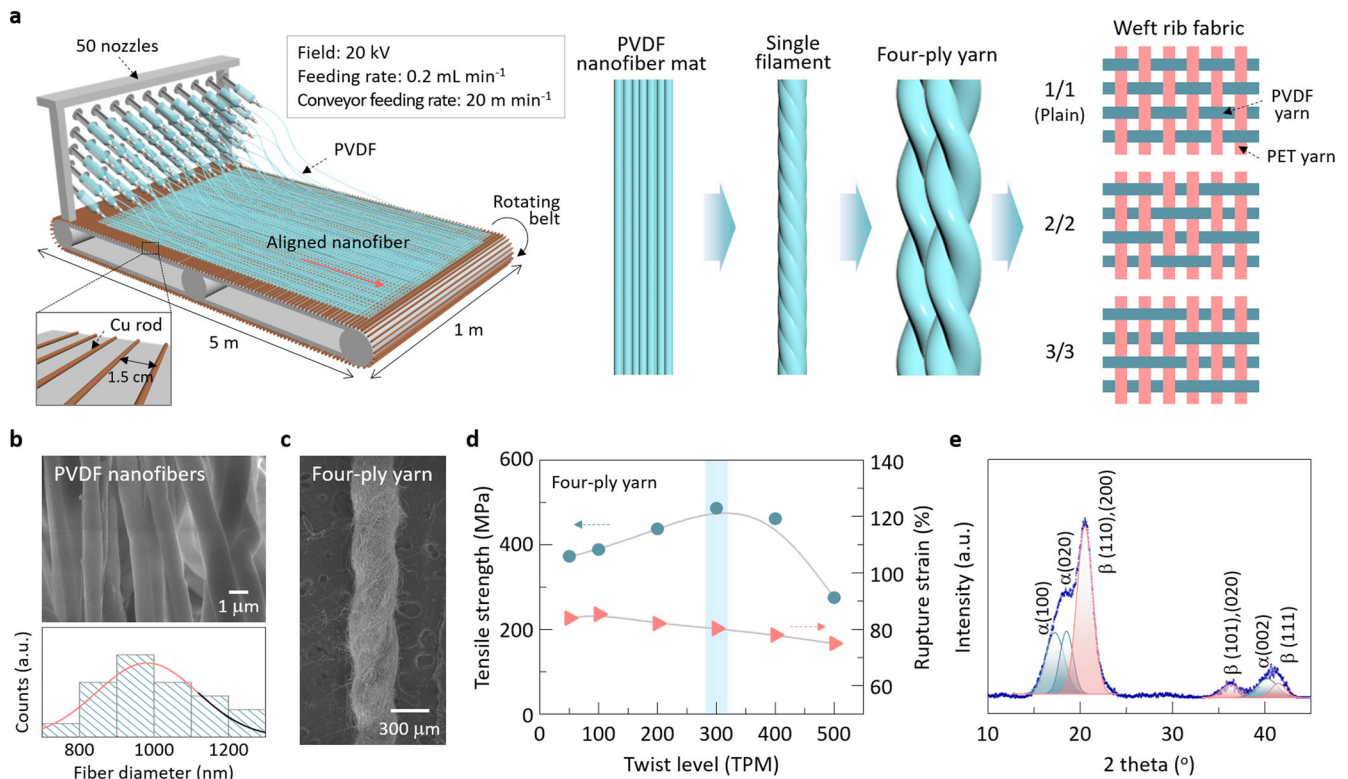


**Fig. 1 Preparation of PVDF yarns and versatile woven fabrics.** **a** Schematic of the 50 nozzle electrospinning process for producing an aligned PVDF nanofiber mat, wherein the Cu rods are positioned in parallel on the conveyor belt, with the steps for preparing three woven structures from four-ply yarns made from a single filament. **b** SEM image of the aligned as-prepared PVDF fibers with the fiber diameter distribution. **c** SEM image of a four-ply yarn. **d** Tensile strength and rupture strain of the four-ply yarn as a function of the twist level. **e** XRD pattern of the four-ply yarn, indicating the presence of  $\alpha$ - and  $\beta$ -phases.

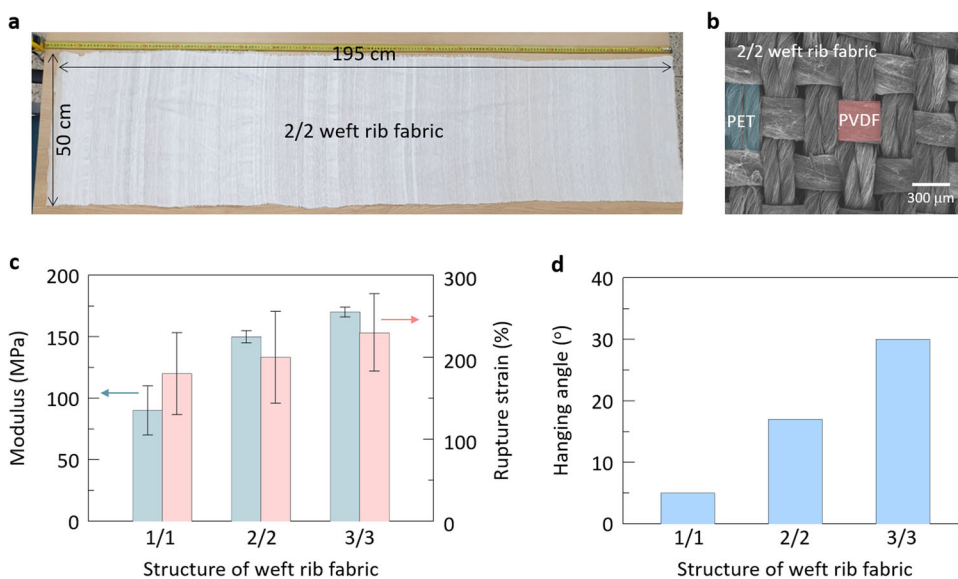


**Fig. 2 Large-area fabric and their physical characteristics.** **a** Photograph of the large-scale woven fabric with the 2/2 weft rib pattern, reaching dimensions of 195 cm × 50 cm. **b** SEM image of the 2/2 weft rib pattern consisting of alternately crossing a single strand of PVDF weft yarn with two strands of PET warp yarn. **c** Modulus and rupture strain of different woven fabrics of 1/1, 2/2, and 3/3 weft rib patterns. **d** Hanging angles measured for the fabrics.

down to form the fabrics, with only a difference in the repeating number of PET yarn in the PVDF weft rib structure.

The tensile strength of the four-ply yarn was optimized by changing the twist level, as shown in Fig. 1d. A maximum tensile strength of ~486 MPa was obtained at a twist level of 300 TPM, indicating that an optimal twist level exists. It is known that the tensile strength of yarns depends on the twist level by two compensating effects: cohesion and obliquity<sup>40,41</sup>. The inter-yarn friction and thus the fiber-to-fiber cohesion are increased with increasing the twist level, owing to the increase of the enlarged resistance against slip (the cohesion effect). However, the twist can impose torsion stress on fibers and possibly decrease the strength (the obliquity effect). With the two compensating effects, a peak value of tensile strength exists depending on the twist level. When it exceeds the optimal twist level, the yarn is exposed to mechanical friction in the excessively twisted fiber structure, which causes damage and breakage, thereby decreasing the tensile strength<sup>42</sup>. The rupture strain was maintained at nearly 80%, implying mechanical suitability for weaving<sup>43</sup>. At the optimal twisting condition of 300 TPM, the average diameter of the four-ply yarn was ~300 μm.

The four-ply PVDF yarn was further characterized through a structural analysis. Figure 1e shows the XRD pattern of the four-ply yarn (twisted at 300 TPM). Strong crystallinity was observed; peaks of  $\alpha$ - and  $\beta$ -phases could be distinguished, with the latter being dominant. Crystalline phases form in PVDF according to the different dipole alignments, namely, antiparallel alignment for the nonpolar  $\alpha$ -phase and parallel alignment for the polar  $\beta$ -phase<sup>18</sup>. It is well known that the  $\beta$ -phase, preferred for high piezoelectricity, is dominantly produced when a high electric field is applied during electrospinning<sup>19</sup>. The relative portion of the  $\beta$ -phase was estimated using the relation of  $\beta$ -phase (%) =  $\frac{A_{\beta}}{A_{\alpha} + A_{\beta}} \times 100$ , where  $A_{\alpha}$  and  $A_{\beta}$  are the areas of the  $\alpha$ - and  $\beta$ -phase peaks, respectively<sup>44</sup>. To calculate  $A_{\alpha}$  and  $A_{\beta}$ , all the peaks in the  $2\theta$  range of 10 to 45° were deconvoluted using a Gaussian function, as shown in Fig. 1e. The amount of the  $\beta$ -phase was estimated to be approximately 55.8%. The dominance of the  $\beta$ -phase was confirmed by the Fourier transform infrared (FTIR) absorption spectrum, as shown in Supplementary Fig. 2. The distinguishable peaks at 840 cm<sup>-1</sup> and 1280 cm<sup>-1</sup> are related to the out-of-plane vibration of the C–F

bonds<sup>45</sup>. Another peak at 880 cm<sup>-1</sup> represents the skeletal vibration of the C–C bonds of the  $\beta$ -phase<sup>46</sup>.

PVDF/PET fabrics with the 1/1, 2/2, and 3/3 weft rib weave patterns were fabricated using a commercial weaving machine. Figure 2a shows an example of the final PVDF/PET fabric with a 2/2 weft rib on a scale of ~195 cm × 50 cm. An example of an SEM image of the 2/2 weft rib weave is shown in Fig. 2b. The mechanically robust 100 μm-thick PET yarns were used in parallel as the warp, whereas the PVDF piezoelectric yarns were inserted as the weft. Owing to the interlacing of warp and weft yarns, weaves form in the fabric, which are called ‘crimps’. The distance between the warp yarns of a crimp was larger than that between adjacent warp yarns. Consequently, the number of warp yarns per unit length increased in the following order: 1/1 < 2/2 < 3/3 weft ribs. Owing to the high tensile modulus of the warp PET yarn, the modulus and rupture strain tended to increase in the same order, as shown in Fig. 2c. The hanging angle also depended on the weaving structure, revealing the highest angle of ~30° in the 3/3 weft rib pattern (Fig. 2d). Photographs of the woven fabrics indicating the measured hanging angles are shown in Supplementary Fig. 3.

### Pressure-sensing performance of versatile piezoelectric fabrics

Using the different fabrics with 1/1, 2/2, and 3/3 weft rib patterns, pressure sensors were fabricated by sandwiching a 2 cm × 2 cm fabric between indium tin oxide (ITO)/PET and Ag-coated nylon fabric, as shown in the device schematic in Supplementary Fig. 4 (along with an image of the actual sensor). An encapsulation layer of polyimide (PI) was applied to both layers with external Cu wires for the electrical measurements. Figure 3a shows the piezoelectric output performance of the fabric sensors with the compressive force increasing from 4 to 24 N, which was applied by finger-pressing at a frequency of 1 Hz. The actual applied force was determined during measurement by attaching a commercial force sensor to the fabric, as presented in Supplementary Fig. 5. As expected, the output voltage and current increased with the increasing force being applied to the PVDF/PET fabrics, regardless of the weave pattern. For example, for the 1/1 weft rib fabric, the maximum output voltage and current increased from ~0.09 V and

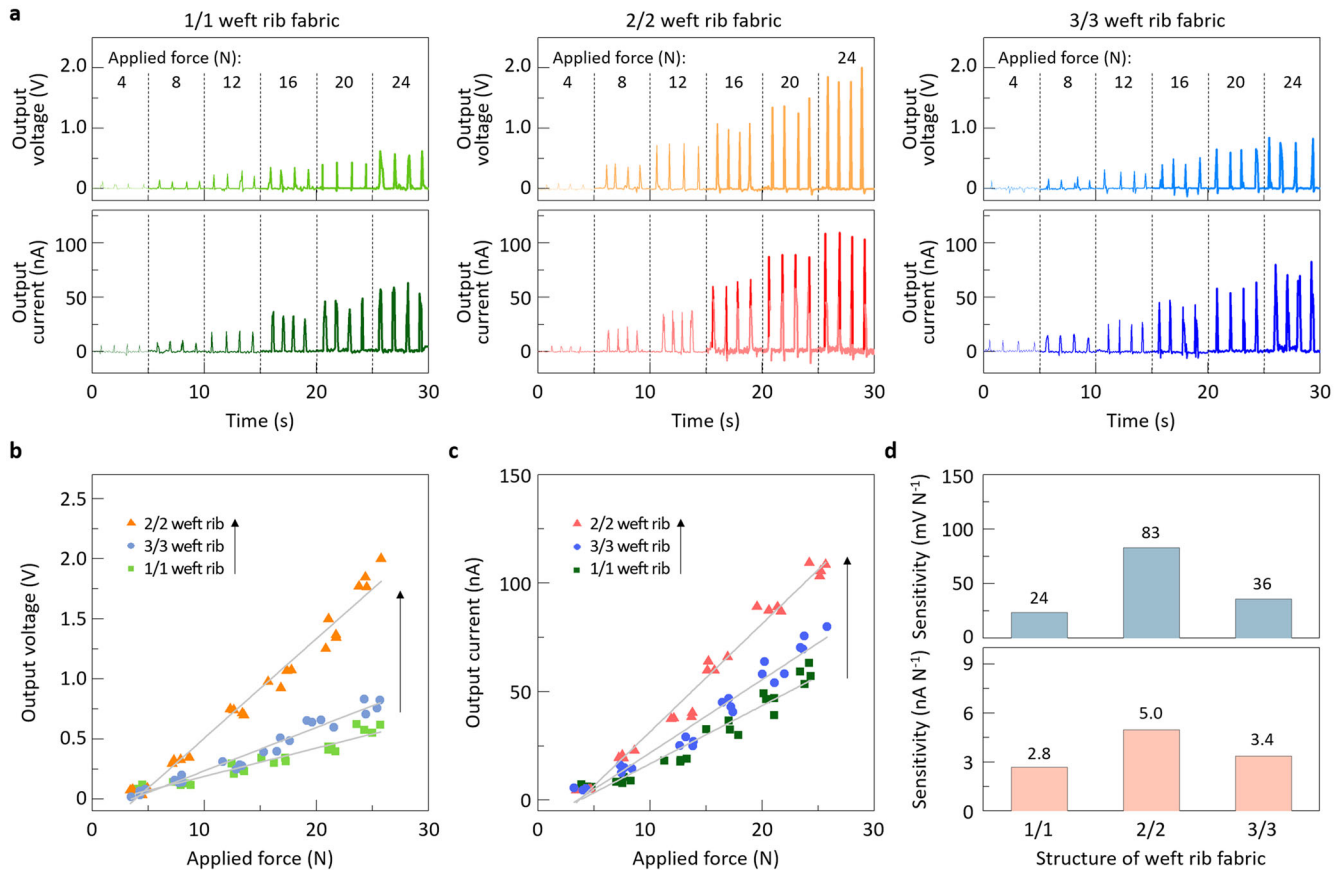


**Fig. 3** Electrical performances of the fabric-based pressure sensor. **a** Output voltage and current generated by finger-pressing the generators incorporating 1/1, 2/2, and 3/3 weft rib weave fabrics over the designated regions applied with the measured forces from ~4 N to ~24 N. **b, c** Plots of peak voltage **b** and current **c** as functions of the applied force monitored by a force sensor attached to each type of fabric. **d** Voltage and current sensitivities measured for the different weave structures.

~7 nA at a force of 4 N to ~0.62 V and ~63 nA at 24 N. The fabric sensors responded consistently during repeated compression as seen in the repeatability test of the 2/2 weft rib pattern up to 1,000 cycles under a finger-taping at ~16 N, which suggests good reliability of the sensing performance as shown in Supplementary Fig. 6.

The dependences of the peak voltage and current on the applied force points are plotted for the three fabric patterns in Fig. 3b, c. Both the voltage and current exhibited nearly linear relationships with the applied force for all the fabric sensors. Notably, higher voltage and current values were observed in the case of the 2/2 weft rib pattern, reaching ~2.0 V and ~109 nA at the maximum force level of ~24 N. Although the maximum voltage and current values may not be critical in sensing applications, broad ranges of peak values are useful in designing wearable fabric sensors depending on the type and magnitude of the input force<sup>47</sup>. It should be mentioned that the stretching of the fabric in the direction of PVDF weft yarn produced a small voltage of ~4.5 mV at the maximum stretching strain of ~25%, indicating that the strain itself has the limitation of creating a significant signal output, as seen in Supplementary Fig. 7.

In addition, the sensitivity values for the voltage and current outcomes were evaluated as seen in Fig. 3d. The sensitivity, i.e., the responding ability per given pressure, was extracted from the slope of the projected lines in each plot, where a larger slope indicates higher sensitivity. As anticipated, high voltage sensitivity values of 83 mV N<sup>-1</sup> and 36 mV N<sup>-1</sup> were attained for the 2/2 and 3/3 weft rib sensors, respectively, which corresponded to increments of ~245% and ~50%, relative to 24 mV N<sup>-1</sup> for the

1/1 weft rib sensor. Similar to the voltage sensitivity, the current sensitivity depended on the fabric pattern, showing an identical increasing tendency: ~2.8 nA N<sup>-1</sup> for 1/1 weft rib fabric, ~3.4 nA N<sup>-1</sup> for 3/3 weft rib fabric, and ~5.0 nA N<sup>-1</sup> for 2/2 weft rib fabric. The voltage sensitivity range is far better than the reported values of 10–20 mV N<sup>-1</sup> for typical commercial quartz-based force sensors<sup>48</sup>. As an example of a similar fabric-based sensor, a plain fabric woven with PVDF and Ag-coated nylon yarns demonstrated a sensitivity of 55 mV N<sup>-1</sup> under periodic impact forces of 70 N at 1 Hz<sup>29</sup>. Another fabric knitted from PVDF yarns reported a sensitivity of ~17.6 mV N<sup>-1</sup> at a compressive pressure of 0.1 MPa<sup>28</sup>.

The dependence of the sensing performance on the fabric pattern may be explained by the differences in the force distributions in the weave structure with applied force. Figure 4 illustrates cross-sectional schematics of the 1/1, 2/2, and 3/3 weft rib fabrics with the potential distribution of crossover contact points between the weft and warp yarns under an external compressive force. The gray lines along the light-blue PVDF weft yarn indicate the original position before applying the vertical compressive pressure. Because electromechanical coupling occurs in the piezoelectric weft yarn upon a physical stimulus, the number of contact points and the magnitude of the resulting compressive strain may be the two main attributes that determine power generation according to the fabric structure. The number of contact points per given length is believed to be highest in the case of the 1/1 weft rib fabric, whereas the magnitude of compressive strain is the maximum in the 3/3 weft rib fabric (indicating the greatest mechanical deformation under an

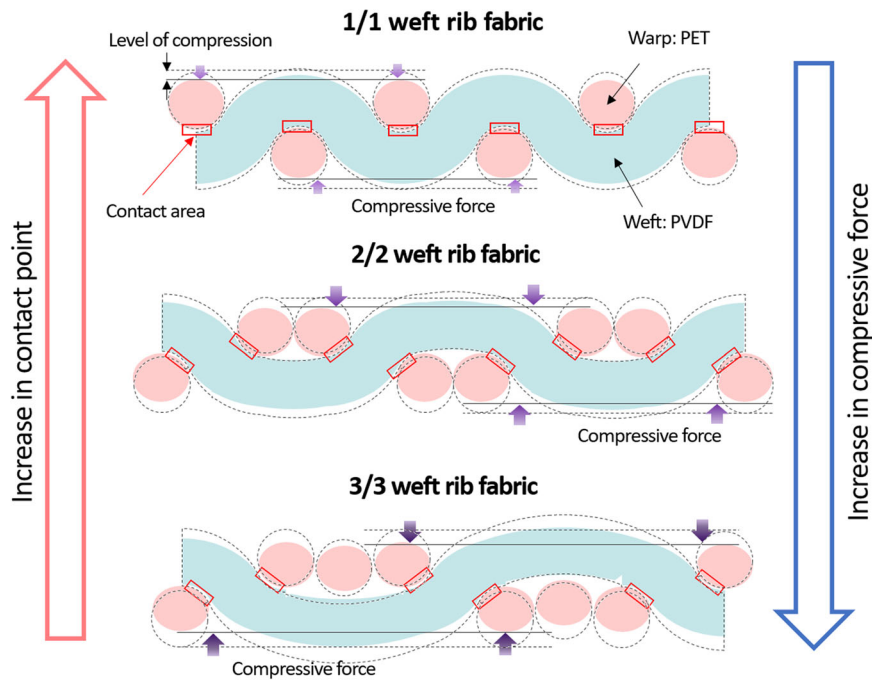


**Fig. 4 Mechanism inducing piezoelectricity in different weave patterns.** Potential mechanism of generating piezoelectricity, which implies the optimal performance of the 2/2 weft rib pattern due to the balance between the effects of the number of contact points and the magnitude of compressive strain.

identical pressure), as illustrated in Fig. 4. With the trade-off relationship between the effects of the number of contact points and compressive strain, the 2/2 weft rib fabric is assumed to perform more optimally in terms of the effectiveness in electromechanical coupling in a pressure sensor, thus leading to the best performance.

#### Extended physiological signal detections using all-fabric sensors

The optimal 2/2 weft rib fabric was further utilized in all-fabric current sensors for real wearable textile electronics, which consist of two sheets of conductive fabric attached to both sides of the piezoelectric fabric and covered with common cotton fabric, as illustrated in Supplementary Fig. 8. Figure 5a shows the piezoelectric responses of the all-fabric sensors under three different mechanical inputs: bending, twisting, and crumpling. As another example of using an all-fabric sensor, Fig. 5b presents the real-time Morse code signals of the word 'YONSEI' using a finger to touch the sensor with long and short pulses. The current generated by these touches can be interpreted as dashes (designated by the pink box) and dots (designated by the blue box). To recognize a dash symbol, for example, a downward peak was created from the first touch in stage I. During the retention stage II, the signal did not reflect any valid information. When the pressure was released in stage III, the signal responded in the opposite direction, i.e., an upward peak. When the output current of the sensor is quickly decreased and increased without stage II, the signal can be regarded as a dot.

In addition, a small block with a mass of 2.025 g (corresponding to  $\sim 0.02$  N) was successfully detected when it was dropped onto the surface of the sensor and then picked up, as demonstrated by the electrical signals in Fig. 5c. The fabric sensor also effectively detected electrical signals from various motions of the human body. Figure 5d shows the output currents generated by the movement of a finger in the all-fabric sensor attached to the finger joints. When the finger bending angle changed from  $\sim 30^\circ$  to  $\sim 120^\circ$ , the output currents varied from 15 to 50 nA, suggesting

that the detected current can indicate the angle of finger bending. The electrical signals produced by the finger motion also depended on the number of finger bends, with the instantaneous signals of each bend (Fig. 5d). The all-fabric sensors monitored foot motions by checking different levels of electrical signals during standing, walking, and running, as shown in Fig. 5e. The output current remained unchanged in the standing posture and increased during walking or running, indicating that the higher impact exerted on the sensor produced greater deformation with a greater electrical response. The above sensing results imply that our proposed all-fabric sensor responds to a wide range of input forces from 0.02 N (a small block dropping) to 694 N (running) in self-powered mode, unlike the cases of capacitive or piezoresistive sensors, as illustrated with various mechanical sources covering the force range in Fig. 5f<sup>49</sup>. It should be mentioned that the drop/pick-up testing using  $\sim 0.02$  N (as seen in Fig. 5c) had the identical result for the fabric sensor after applying the maximum force of 694 N as seen in Supplementary Fig. 9, indicating good recovering capability of the fabric.

A piece of the best 2/2 weft rib fabric with dimensions of  $\sim 5.5$  cm  $\times$   $\sim 20$  cm was further incorporated into a shoe insole with a printed electrode pattern, with two focused areas at the front and heel parts. Our PVDF/PET fabric-based pressure sensor exhibited promising sensing performance, even in detecting walking motion with a photograph in Fig. 6a<sup>50</sup>. As shown in Fig. 6b-d, all walking steps, such as heel-strike, support, toe-contact, and leg-lift, were detected using piezoelectric signals. Different output signal peaks were detected depending on the magnitude of the pressure for each gait based on the working mechanisms of the piezoelectric sensor<sup>51</sup>. These results may indicate the superior sensing ability of the all-fabric-based piezoelectric sensors with design flexibility considering various input stimuli. It should be mentioned that voltage as an output signal was used in Fig. 6, instead of current in Fig. 5, to demonstrate that both the voltage and current can be used as output signals in the fabric sensors as reported similarly<sup>8,52</sup>. To evaluate the durability of the all-fabric sensor, the devices were washed up to five times using an automatic laundry machine, and

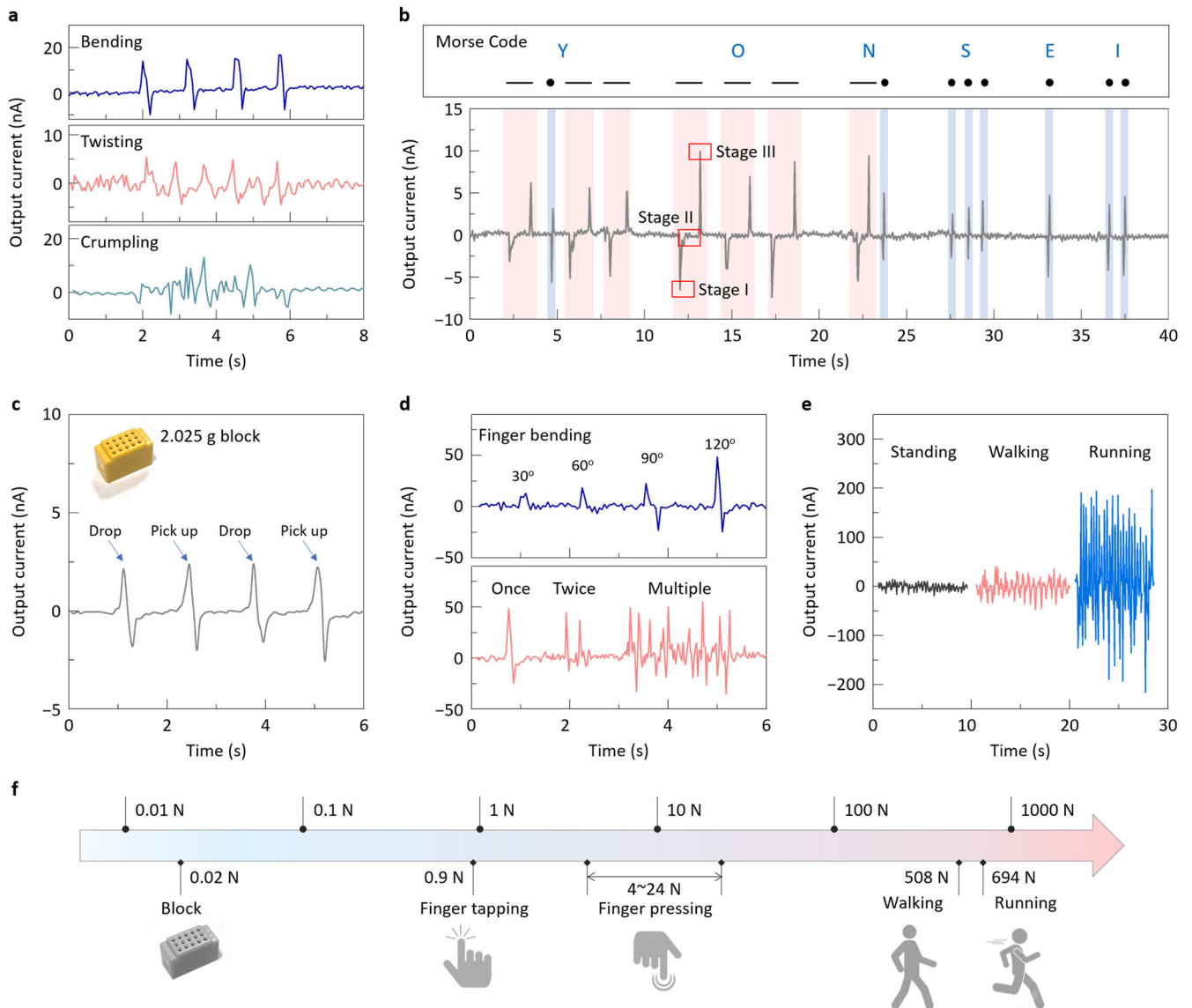


**Fig. 5 Sensing performances of all-fabric-based pressure sensors.** **a** Current-sensing performance of the 2/2 weft rib weave generator during manual bending, twisting, and crumpling motions. **b** Examples of Morse codes created by finger-pressing operations with three stages of operation: stage I for the negative signal, stage II for the null current, and stage III for the positive signal. **c** Generation of an output current by dropping and picking up a small block. **d** Output current signals produced by finger-bending with different bending angles (top) and the number of finger bends (bottom). **e** Current generated by foot motions of walking and running compared with that of the standing position. **f** Schematic illustration of various mechanical input sources for the wide pressure range of  $10^{-2}$  to  $10^3$  N.

the change in the current signal after each washing is shown in Supplementary Fig. 10. Washability is an important evaluation parameter for any fabric-based wearable sensor<sup>53</sup>. After standard washing five times, ~81.3% of output current was maintained, indicating the fabric is as durable as regular cloth.

All fabric-based sensors can be easily customized into large pressure sensors to monitor the distribution of mechanical input stimuli. Figure 6e shows a schematic of an all-fabric sensor with an array of  $4 \times 3$  touch pixels with an area of  $1.5 \times 1.5$  cm<sup>2</sup> each (with a photograph of an actual sensor in Supplementary Fig. 11). Each pixel exhibits a similar response with an average voltage signal of  $0.51 \pm 0.04$  V, as depicted in the three-dimensional distribution of electrical signals in Fig. 6f. Further, the finger touching of each pixel unit was monitored to determine whether electrical crosstalk was prevented as seen in the detected signals at the selected pixels. For example, as shown in Fig. 6g, when a finger applied pressure to pixel 1, it responded, whereas other pixels did not.

Similarly, none of the pixels responded when pixel 3 was pressed, verifying that there was no electrical or mechanical crosstalk between neighboring pixels.

## DISCUSSION

High-sensitivity and wearable all-fabric-based pressure sensors incorporating piezoelectric PVDF nanofiber yarn were successfully demonstrated, with the capability of detecting a wide range of input forces up to 694 N. Fifty nozzles on a single prototype electrospinner were used to produce a continuous nanofiber mat with the help of intermittent Cu rods on a moving carrier for fiber alignment. The as-spun fibers were subsequently spun into four-ply PVDF yarn to ultimately weave a large-scale fabric of  $\sim 195$  cm  $\times$   $\sim 50$  cm using commercial PET yarn for the warp. The optimized fabric with a 2/2 weft rib pattern showed a sensitivity of  $83$  mV N<sup>-1</sup> under periodic compression, which corresponds to

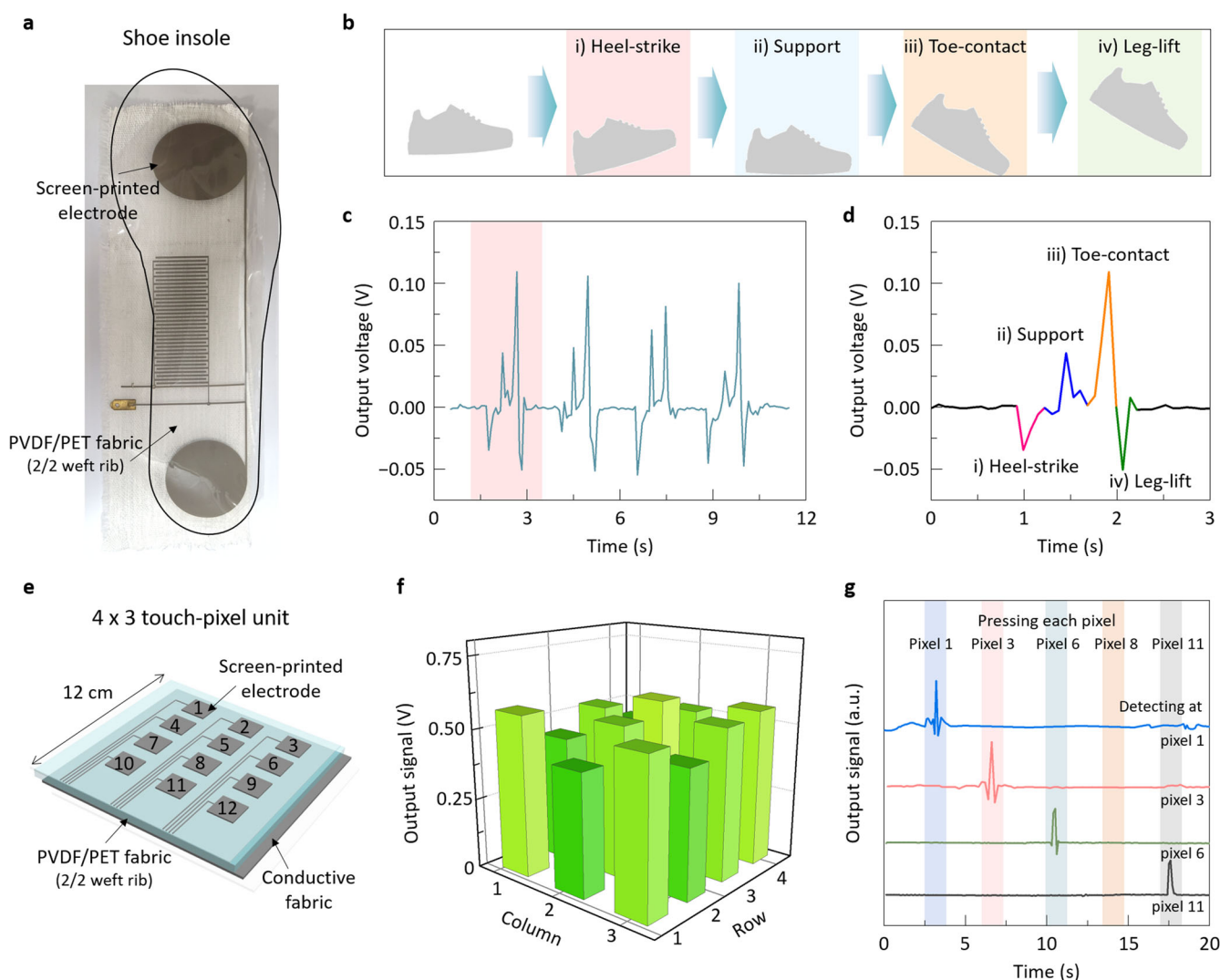


**Fig. 6** Extended applications of all-fabric pressure sensors. **a** Example of a shoe-insole pressure sensor fabricated from the 2/2 weft rib fabric, which was inserted below two circular electrodes to detect the front (just below the toes) and heel motions. **b** Schematic illustrations of each stage of a single step during walking: heel-strike, support, toe-contact, and leg-lift. **c** Output voltage signals in response to each part of a walking step for gait analysis, and **d** the magnified electrical signals correlated with each stage in a step. **e** Schematic of all-fabric pressure sensors with an array of box-type pixel units numbered up to 12, with the conductor lines patterned for detecting separate signal from each pixel. **f** Three-dimensional plots of electrical signals produced by finger-pressing of each pixel. **g** Electrical signals detected only at the pixel pressed by finger, without the creation of side-signals at other pixels, confirming no cross-talk.

an increase of  $\sim 245\%$  relative to the reference 1/1 weft rib case. Various physiological motions including bending, twisting, crumpling, walking, and running were successfully monitored with distinguishable electrical signals using the resulting all-fabric-based pressure sensors. The all-fabric-sensor also exhibited comparable durability to a regular cloth, retaining  $\sim 81.3\%$  of the original output current after five standard washes. A fabric pressure sensor with a  $4 \times 3$  array of touch pixels showed similar piezoelectric signals in all pixels, with an average output voltage of  $0.51\text{ V}$  and a low standard deviation of  $\pm 0.04\text{ V}$ . The optimal fabric sensor was also proven to be highly effective for health monitoring by producing electrical signals that correlated with sequential human walking segments.

## METHODS

### Preparation of the PVDF/PET-yarn-based fabrics

A PVDF precursor solution was prepared by dissolving 19 wt.% PVDF powder (Kynar flex-2801-00, Piezotech, France) relative to 100 wt.% of a

mixed solvent of dimethyl sulfoxide (DMSO, 99.5%, Sigma-Aldrich, USA) and acetone (99.5%, Duksan, Republic of Korea). The solution became clear after stirring overnight at a fixed temperature of  $60^\circ\text{C}$ . The precursor solution was electrospun using a customized multinozzle electrospinner that incorporates 50 needle-spinnerets with hole-opening diameters  $\sim 0.57\text{ mm}$ . The nanofibers were continuously ejected through the spinnerets onto a conveyor belt at a speed of  $0.2\text{ mL min}^{-1}$  under a constant electric field of  $\sim 20\text{ kV}$ . The Cu rods with an interval of  $\sim 1.5\text{ cm}$  were arrayed on the entire belt, perpendicular to the direction of the rotating belt, to aid the alignments of nanofibers when they settled down onto the belt. The resultant nanofiber mat was merged into a single filament ( $\sim 120\ \mu\text{m}$  in diameter). The final four-ply yarn ( $\sim 300\ \mu\text{m}$  in diameter) was prepared by drawing/twisting four single-filament yarns at a draw ratio of 2.35 with a variable twist level of 50 to 500 TPM. Using a customized rapier loom (Sambo Eng. Co., Korea), these yarns were then woven into three different fabric structures, that is, 1/1 (plain), 2/2, and 3/3 weft rib weaves, in which PVDF and PET yarns were used as the weft and warp, respectively, in the resultant tapestry. For example, the 2/2 weft rib weave is a woven fabric wherein one strand of PVDF weft yarn crosses two alternating strands of PET warp yarns up and down in the rib fabric.

The fabrics were woven at the weft insertion speed of 50 picks per minute with the reed width of 50 cm.

### Characterization of yarns and fabrics

The morphologies of the four-ply yarn and PVDF/PET fabrics were observed via scanning electron microscopy (SEM; JEOL-7610, JEOL, Japan). A two-dimensional FFT was performed using ImageJ software to determine the distribution of the as-spun fiber orientations. The crystallographic phase of the PVDF yarn was identified using X-ray diffractometry (XRD, SmartLab, Rigaku, Japan) with Cu K $\alpha$  radiation. The PVDF yarns were also analyzed using FTIR spectroscopy (Vertex 70, Bruker, USA) in the frequency range 700–1800 cm<sup>-1</sup>. The tensile strength and rupture strain of the PVDF yarn were measured using a universal testing machine on the basis of ASTM D2256. Mechanical properties of the PVDF/PET fabrics were estimated for the five fabric samples with 50 mm width and 150 mm height in accordance of ASTM D5035. The hanging angles of PVDF/PET fabrics were determined using a metal horizontal platform as following ASTM D1388-07.

### Fabrication and measurement of pressure sensors

Piezoelectric pressure sensors were constructed using the PVDF/PET textiles (2 cm  $\times$  2 cm) with different woven structures by employing an Ag-coated nylon fabric as the top electrode and an ITO-coated PET film as the bottom electrode. Cu wires were then connected to the top and bottom electrodes, and a PI film was used to encapsulate the device. The output voltage and current were measured with input forces applied by finger-pressing using a nanovoltmeter (Keithley 2182 A, ValueTronics, USA: internal resistance of 10 M $\Omega$ ) and a galvanostat system (IviumStat, Ivium Technologies, Netherlands: internal resistance of 1 M $\Omega$ ), respectively. The magnitude of the applied force was monitored during the measurements using a tactile pressure sensor (FlexiForce A201, Nitta, Japan) attached to the device. In addition, all-fabric-based pressure sensors measuring 4 cm  $\times$  4 cm were assembled using the 2/2 weft rib fabric, wherein the bottom electrode was replaced with an Ag-coated nylon fabric (LXG-1, Soitex, Korea: resistance of 0.8  $\Omega$ ) instead of ITO/PET. The pressure sensors were also applied to a large-area (12 cm  $\times$  12 cm) fabric sandwiched between two cotton cloths, which had an arrayed electrode pattern of screen-printed Ag to complete the fabric-based touch sensor. Electrical signals produced by the foot during various stages of human walking were further detected using a patterned mask in the shape of a shoe insole (Sang-A Frontec, Republic of Korea).

### DATA AVAILABILITY

The data that support the findings of this study are available from the corresponding authors upon reasonable request.

Received: 13 April 2022; Accepted: 19 July 2022;

Published online: 05 August 2022

### REFERENCES

- Shehazd, M., Wang, S. & Wang, Y. Flexible and transparent piezoelectric loudspeaker. *npj Flex. Electron.* **5**, 24 (2021).
- Choi, H. J., Jung, Y. S., Han, J. & Cho, Y. S. In-situ stretching strain-driven high piezoelectricity and enhanced electromechanical energy-harvesting performance of a ZnO nanorod-array structure. *Nano Energy* **72**, 104735 (2020).
- Kim, D. B., Park, K. H. & Cho, Y. S. Origin of high piezoelectricity of inorganic halide perovskite thin films and their electromechanical energy-harvesting and physiological current-sensing characteristics. *Energy Environ. Sci.* **13**, 2077–2086 (2020).
- Cho, A., Kim, D. B. & Cho, Y. S. Electric-field-dependent surface potentials and vibrational energy-harvesting characteristics of Bi(Na<sub>0.5</sub>Ti<sub>0.5</sub>)O<sub>3</sub>-based Pb-free piezoelectric thin films. *ACS Appl. Mater. Interfaces* **11**, 13244–13250 (2019).
- Kim, D. B., Jo, K. S., Park, S. J. & Cho, Y. S. Contribution of anisotropic lattice-strain to piezoelectricity and electromechanical power generation of flexible inorganic halide thin films. *Adv. Energy Mater.* **12**, 2103329 (2022).
- Sultana, A. et al. Organo-lead perovskite regulated green light emitting poly(vinylidene fluoride) electrospun nanofiber mat and its potential utility for ambient mechanical energy harvesting application. *Nano Energy* **49**, 380–392 (2018).
- Song, K., Zhao, R., Wang, Z. L. & Yang, Y. Conjoined pyro-piezoelectric effect for self-powered simultaneous temperature and pressure sensing. *Adv. Mater.* **31**, 1902831 (2019).
- Han, J. et al. Origin of high piezoelectricity in carbon nanotube/halide nanocrystal/P(VDF-TrFE) composite nanofibers designed for bending-energy harvesters and pressure sensors. *Nano Energy* **99**, 107421 (2022).
- Wang, Y. et al. Hierarchically patterned self-powered sensors for multifunctional tactile sensing. *Sci. Adv.* **6**, eabb9083 (2020).
- Yang, Y. et al. Polyimide/graphene nanocomposite foam-based wind-driven triboelectric nanogenerator for self-powered pressure sensor. *Adv. Mater. Technol.* **4**, 1800723 (2019).
- Han, J. et al. Origin of enhanced piezoelectric energy harvesting in all-polymer-based core-shell nanofibers with controlled shell-thickness. *Compos. Part B Eng.* **223**, 109141 (2021).
- Kim, D. B., Kim, S. W., Kim, Y. E., Choi, H. J. & Cho, Y. S. Room-temperature processed Ag/Pb(Zn<sub>1/3</sub>Nb<sub>2/3</sub>)O<sub>3</sub>-Pb(Zr<sub>0.5</sub>Ti<sub>0.5</sub>)O<sub>3</sub>-based composites for printable piezoelectric energy harvesters. *Compos. Sci. Technol.* **218**, 109151 (2022).
- Hosseini, E. S., Manjakkal, L., Shakhthivel, D. & Dahiya, R. Glycine-chitosan-based flexible biodegradable piezoelectric pressure sensor. *ACS Appl. Mater. Interfaces* **12**, 9008–9016 (2020).
- Li, T. et al. Pure OPM nanofibers with high piezoelectricity designed for energy harvesting in vitro and in vivo. *J. Mater. Chem. B* **6**, 5343–5352 (2018).
- Chang, C., Tran, V. H., Wang, J., Fuh, Y. K. & Lin, L. Direct-write piezoelectric polymeric nanogenerator with high energy conversion efficiency. *Nano Lett.* **10**, 726–731 (2010).
- Jia, N., He, Q., Sun, J., Xia, G. & Song, R. Crystallization behavior and electroactive properties of PVDF, P(VDF-TrFE) and their blend films. *Polym. Test.* **57**, 302–306 (2017).
- Mondal, S., Paul, T., Maiti, S., Das, B. K. & Chattopadhyay, K. K. Human motion interactive mechanical energy harvester based on all inorganic perovskite-PVDF. *Nano Energy* **74**, 104870 (2020).
- Ruan, L. et al. Properties and applications of the  $\beta$  phase poly(vinylidene fluoride). *Polymers* **10**, 228 (2018).
- Ju, B. J., Oh, J. H., Yun, C. & Park, C. H. Development of a superhydrophobic electrospun poly(vinylidene fluoride) web via plasma etching and water immersion for energy harvesting applications. *RSC Adv.* **8**, 28825–28835 (2018).
- Wang, Y., Yokota, T. & Someya, T. Electrospun nanofiber-based soft electronics. *NPJ Asia Mater.* **13**, 22 (2021).
- Ico, G. et al. Size-dependent piezoelectric and mechanical properties of electrospun P(VDF-TrFE) nanofibers for enhanced energy harvesting. *J. Mater. Chem. A* **4**, 2293–2304 (2016).
- Liu, K. et al. Piezoelectric energy harvesting and charging performance of Pb(Zn<sub>1/3</sub>Nb<sub>2/3</sub>)O<sub>3</sub>-Pb(Zr<sub>0.5</sub>Ti<sub>0.5</sub>)O<sub>3</sub> nanoparticle-embedded P(VDF-TrFE) nanofiber composite sheets. *Compos. Sci. Technol.* **168**, 296–302 (2018).
- Shi, K., Sun, B., Huang, X. & Jiang, P. Synergistic effect of graphene nanosheet and BaTiO<sub>3</sub> nanoparticles on performance enhancement of electrospun PVDF nanofiber mat for flexible piezoelectric nanogenerators. *Nano Energy* **52**, 153–162 (2018).
- Sultana, A. et al. Methylammonium lead iodide incorporated poly(vinylidene fluoride) nanofibers for flexible piezoelectric-pyroelectric nanogenerator. *ACS Appl. Mater. Interfaces* **11**, 27279–27287 (2019).
- Kang, H. B. et al. (Na,K)NbO<sub>3</sub> nanoparticle-embedded piezoelectric nanofiber composites for flexible nanogenerators. *Compos. Sci. Technol.* **111**, 1–8 (2015).
- Eun, J. H., Sung, S. M., Kim, M. S., Choi, B. K. & Lee, J. S. Effect of MWCNT content on the mechanical and piezoelectric properties of PVDF nanofibers. *Mater. Des.* **206**, 109785 (2021).
- Talbourdet, A. et al. 3D interlock design 100% PVDF piezoelectric to improve energy harvesting. *Smart Mater. Struct.* **27**, 075010 (2018).
- Soin, N. et al. Novel “3-D spacer” all fibre piezoelectric textiles for energy harvesting applications. *Energy Environ. Sci.* **7**, 1670–1679 (2014).
- Magniez, K., Krajewski, A., Neuenhofer, M. & Helmer, R. Effect of drawing on the molecular orientation and polymorphism of melt-spun poly(vinylidene fluoride) fibers: Toward the development of piezoelectric force sensors. *J. Appl. Polym. Sci.* **129**, 2699–2706 (2013).
- Lund, A. et al. Energy harvesting textiles for a rainy day: Woven piezoelectrics based on melt-spun PVDF microfibrils with a conducting core. *npj Flex. Electron.* **2**, 9 (2018).
- Åkerfeldt, M., Nilsson, E., Gillgard, P. & Walkenström, P. Textile piezoelectric sensors—melt spun bi-component poly(vinylidene fluoride) fibres with conductive cores and poly(3,4-ethylene dioxathiophene)-poly(styrene sulfonate) coating as the outer electrode. *Fash. Text.* **1**, 13 (2014).
- Zhou, Y. et al. Highly sensitive, self-powered and wearable electronic skin based on pressure-sensitive nanofiber woven fabric sensor. *Sci. Rep.* **7**, 12949 (2017).
- Yang, E. et al. Nanofibrous smart fabrics from twisted yarns of electrospun piezopolymer. *ACS Appl. Mater. Interfaces* **9**, 24220–24229 (2017).
- Zhao, Z. et al. Machine-washable textile triboelectric nanogenerators for effective human respiratory monitoring through loom weaving of metallic yarns. *Adv. Mater.* **28**, 10267–10274 (2016).



35. Zhang, J. M. et al. Preparation of high modulus poly(ethylene terephthalate): influence of molecular weight, extrusion, and drawing parameters. *Int. J. Polym. Sci.* **2017**, 2781425 (2017).
36. Kim, J. I., Hwang, T. I., Aguilar, L. E., Park, C. H. & Kim, C. S. A controlled design of aligned and random nanofibers for 3D bi-functionalized nerve conduits fabricated via a novel electrospinning set-up. *Sci. Rep.* **6**, 23761 (2016).
37. Li, D., Wang, Y. & Xia, Y. Electrospinning of polymeric and ceramic nanofibers as uniaxially aligned arrays. *Nano Lett.* **3**, 1167–1171 (2003).
38. Katta, P., Alessandro, M., Ramsier, R. D. & Chase, G. G. Continuous electrospinning of aligned polymer nanofibers onto a wire drum collector. *Nano Lett.* **4**, 2215–2218 (2004).
39. Persano, L. et al. High performance piezoelectric devices based on aligned arrays of nanofibers of poly (vinylidene fluoride-co-trifluoroethylene). *Nat. Commun.* **4**, 1633 (2013).
40. Zhou, Y., Fang, J., Wang, X. & Lin, T. Strip twisted electrospun nanofiber yarns: Structural effects on tensile properties. *J. Mater. Res.* **27**, 537–544 (2011).
41. Singh, J. I. P., Dhawan, V., Singh, S. & Jangid, K. Study of effect of surface treatment on mechanical properties of natural fiber reinforced composites. *Mater. Today.: Proc.* **4**, 2793–2799 (2017).
42. Park, S. et al. Poling-free spinning process of manufacturing piezoelectric yarns for textile applications. *Mater. Des.* **179**, 107889 (2019).
43. Mishra, S. Effect of construction on strain distribution in woven fabrics under uniaxial tensile deformation. *J. Eng. Fibers Fabr.* **8**, 19–29 (2013).
44. Kim, Y. J., Ahn, C. H., Lee, M. B. & Choi, M. S. Characteristics of electrospun PVDF/SiO<sub>2</sub> composite nanofiber membranes as polymer electrolyte. *Mater. Chem. Phys.* **127**, 137–142 (2011).
45. Janakiraman, S., Surendran, A., Ghosh, S., Anandhan, S. & Venimadhav, A. Electroactive poly(vinylidene fluoride) fluoride separator for sodium ion battery with high coulombic efficiency. *Solid State Ion.* **292**, 130–135 (2016).
46. Jeong, H. G., Han, Y. S., Jung, K. H. & Kim, Y. J. Poly (vinylidene fluoride) composite nanofibers containing polyhedral oligomeric silsesquioxane–epigallocatechin gallate conjugate for bone tissue regeneration. *Nanomaterials* **9**, 184 (2019).
47. Zhu, M., Chng, S. S., Cai, W., Liu, C. & Du, Z. Piezoelectric polymer nanofibers for pressure sensors and their applications in human activity monitoring. *RSC Adv.* **10**, 21887–21894 (2020).
48. Gao, S., Weng, L., Deng, Z., Wang, B. & Huang, W. Biomimetic tactile sensor array based on magnetostrictive materials. *IEEE Sens. J.* **21**, 13116–13124 (2021).
49. Zhang, Z. H. et al. Sensitivity enhancement of piezoelectric force sensors by using multiple piezoelectric effects. *AIP Adv.* **6**, 075320 (2016).
50. Yang, T. et al. Hierarchically structured PVDF/ZnO core-shell nanofibers for self-powered physiological monitoring electronics. *Nano Energy* **72**, 104706 (2020).
51. Zhang, Z. et al. Deep learning-enabled triboelectric smart socks for IoT-based gait analysis and VR applications. *npj Flex. Electron.* **4**, 29 (2020).
52. Peng, X. et al. A breathable, biodegradable, antibacterial, and self-powered electronic skin based on all-nanofiber triboelectric nanogenerators. *Sci. Adv.* **6**, eaba9624 (2020).
53. Fan, W. et al. Machine-knitted washable sensor array textile for precise epidermal physiological signal monitoring. *Sci. Adv.* **6**, eaay2840 (2020).

## ACKNOWLEDGEMENTS

This work was financially supported by grants from the National Research Foundation of Korea (NRF-2016M3A7B4910151 and NRF-2021R1A2C2013501).

## AUTHOR CONTRIBUTIONS

S.M.S., M.S.K., B.K.C., and H.R.H. fabricated fabric samples and performed characterization. D.B.K., J.H., S.J.P., and H.J.C. conducted sensor fabrication and various measurements. B.K.K., C.H.P., and J.H.P. analyzed and interpreted the data. D.B.K. and J.H. wrote the main part of the manuscript. J.L. and Y.S.C., supervised the overall research and completed the manuscript.

## COMPETING INTERESTS

The authors declare no competing interests.

## ADDITIONAL INFORMATION

**Supplementary information** The online version contains supplementary material available at <https://doi.org/10.1038/s41528-022-00203-6>.

**Correspondence** and requests for materials should be addressed to Joon-Seok Lee or Yong Soo Cho.

**Reprints and permission information** is available at <http://www.nature.com/reprints>

**Publisher's note** Springer Nature remains neutral with regard to jurisdictional claims in published maps and institutional affiliations.



**Open Access** This article is licensed under a Creative Commons Attribution 4.0 International License, which permits use, sharing, adaptation, distribution and reproduction in any medium or format, as long as you give appropriate credit to the original author(s) and the source, provide a link to the Creative Commons license, and indicate if changes were made. The images or other third party material in this article are included in the article's Creative Commons license, unless indicated otherwise in a credit line to the material. If material is not included in the article's Creative Commons license and your intended use is not permitted by statutory regulation or exceeds the permitted use, you will need to obtain permission directly from the copyright holder. To view a copy of this license, visit <http://creativecommons.org/licenses/by/4.0/>.

© The Author(s) 2022